Materials & Design 250 (2025) 113584

Contents lists available at ScienceDirect

Materials & Design

journal homepage: www.elsevier.com/locate/matdes

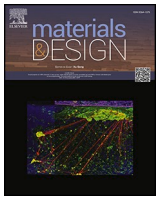

Microstructure, mechanical properties, thermal decomposition and oxidation sequences of crystalline AlB_2 thin films

Chun Hu [a,*], Stanislav Mráz [b], Peter J. Pöllmann [b], T. Wojcik [a], M. Podsednik [c,d], B. Hajas [a], A. Limbeck [c], Nikola Koutná [a,e], Jochen M. Schneider [b], Paul H. Mayrhofer [a]

[a] Institute of Materials Science and Technology, TU Wien, Getreidemarkt 9, Vienna A-1060, Austria
[b] Materials Chemistry, RWTH Aachen University, Kopernikusstr. 10, D-52074 Aachen, Germany
[c] Institute of Chemical Technologies and Analytics, TU Wien, A-1060 Wien, Austria
[d] KAI Kompetenzzentrum Automobil- und Industrieelektronik GmbH, Technologiepark Villach Europastraße 8, A-9524 Villach, Austria
[e] Department of Physics, Chemistry, and Biology (IFM), Linköping University, Linköping SE-58183, Sweden

ARTICLE INFO

Keywords:
AlB_2 thin film
Microstructure
Thermal stability
Oxidation resistance
Ab initio

ABSTRACT

Despite AlB_2 is the most typical structure prototype of transition metal diborides (TMB_2), studies on AlB_2 thin films are scarce. Furthermore, although Al is the primary alloying element for TMB_2 to improve their oxidation resistance, no such data are available for AlB_2 thin films. Here, we develop AlB_x thin films through non-reactive magnetron sputtering of an AlB_2 compound target and investigate their microstructure, mechanical properties, thermal stability and oxidation resistance. Keeping the substrate temperature at 700 °C and increasing the Ar pressure during deposition from $p_{Ar} = 0.4$ to 0.8 to 1.2, Pa, the films' chemistry slightly varies between $x = 1.99$, 1.97, and to 2.27, respectively. Detailed transmission electron microscopy shows that the highly (0001)-oriented $AlB_{2.27}$ thin film exhibits small platelet-like amorphous B regions next to the large columnar α-structured AlB_2 crystals. In the as deposited state, this film exhibits an indentation hardness and elastic modulus of 19.2 ± 1.2 GPa and 331.8 ± 14.4 GPa, respectively. Between 850 and 900 °C, the $AlB_{2.27}$ thin film starts to decompose into tetragonal (t-) AlB_{12}, but still maintains dominant α structure up to 950 °C. At 1000 °C, the thin film is completely decomposed into t-AlB_{12} and hexagonal AlB_{10}. The $AlB_{2.27}$ thin film also shows exceptional oxidation-resistance with an onset temperature for the formation of oxides (α-Al_2O_3 and o-$Al_{18}B_4O_{33}$) between 950 and 1000 °C when exposed to lab-air.

1. Introduction

Transition metal diboride (TMB_2) thin films are technologically important materials exhibiting high hardness and thermal conductivity as well as outstanding chemical inertness [1–3]. The diborides of group 4–6 TMs (Ti [4–6], Zr [7,8], Hf [9], V [10], Nb [11], Ta [12], Cr [13], Mo [14], and W [15]) typically reveal a predominant AlB_2-type crystal structure (space group 191-P6/mmm). However, a strong limitation of TMB_2s is their relatively low oxidation resistance [3]. Among possible strategies for improving oxidation behavior of TMB_2 is Al-addition. Aluminum can, in principle, not only retard oxidation through formation of the protective Al_2O_3 oxide scale [16,17], but also promote age-hardening, as predicted by *ab initio* density functional theory (DFT) calculations [18].

An excellent example is TiB_2—the most widely researched TMB_2 thin film—in which Al-incorporation significantly improves oxidation resistance [16,17,19] and contributes to age-hardening phenomena. At the onset temperature of ~400 °C, $TiB_{2.4}$ forms a highly porous Ti oxide scale due to the evaporation of B_2O_3 (*g*) phase and the coarsening of TiO_2 crystallites [16]. The addition of Al contributes to the formation of a dense, protective Al-containing oxide scale, thus significantly improving the oxidation resistance. In particular, a hardness increase from 32.1 to 37.0 GPa was reported for $(Ti_{0.71}Al_{0.29})B_{2+1.08}$ when annealed at 1000 °C for 1h, due to the phase separation within the (Ti,Al)B_2 columns including the formation of Ti-deficient crystallites within the grain interior [20]. Increasing interest in Al-containing diborides is also illustrated by recently synthesized (Ta,Al)B_2 [21,22], (W,Al)B_2 [23], and (Re,Al)B_2 [24] thin films. For instance, Al-addition into ReB_2 significantly improves the chemical stability upon exposure to air [24]. (Re,Al)B_2 thin film reveals self-passivating phenomenon related to the

* Corresponding author.
E-mail address: chun.hu@tuwien.ac.at (C. Hu).

https://doi.org/10.1016/j.matdes.2025.113584
Received 27 June 2024; Received in revised form 10 December 2024; Accepted 2 January 2025
Available online 3 January 2025

formation of Al-oxide layer, which can withstand corrosion in a time period ≥ 60 days. By contrast, the ReB_2 film already forms $HReO_4$ after two days.

Despite beneficial effects of Al-addition and the fact that AlB_2 is the phase prototype of the α structure—commonly referred to as the AlB_2-type structure and representing the most frequent structure of intermetallic binary and ternary borides [25]—systemic studies on the α-structured AlB_2 thin films are still missing. Here and consistently in the manuscript, we use the symbol α to indicate the AlB_2 phase. Note that some TMB_2s can also crystallize in the WB_2-type phase (denoted by ω, in line with Euchner and Mayrhofer [26]). From modeling perspective, α-AlB_2 has been studied by DFT calculations [25,27–31] showing mechanical and dynamic stability [25,27]. Worth noting, however, is a large scatter of DFT-calculated formation enthalpies [23,28,30,32] and elastic constants, C_{ij}, particularly the off-diagonal C_{12} and C_{13} (e.g., $C_{12} = -3$ GPa [30], $C_{12} = 17$ GPa [29] $C_{12} = 79$ GPa [27]), resulting in Young's moduli of 245–369 GPa [26,28,29]. Lattice dynamics calculations by Johansson et al. [27] indicate that α-AlB_2 is stable only in a narrow composition range, $2.157 \leq x \leq 2.212$ for AlB_x. The Al–B phase diagram, shows the appearance of AlB_2 as a line compound and its decomposition at 956 ± 5 °C [33]. From experimental perspective, Whittaker et al. [34] revealed O_2-pressure-independent oxidation kinetics of AlB_2 powder using thermal gravimetric analysis, but the powder also had 6 wt% Al as secondary phase. Hahn et al. [23] showed that sputtering AlB_2 target leads to amorphous films. Nashimoto et al. [35] also reported the synthesis of X-ray amorphous AlB_2 thin films by rf magnetron sputtering, which can be crystallized after annealing at 700 °C. Thus, systematic studies on mechanical properties and oxidation behavior of α-AlB_2 are essential to facilitate rational design of Al-containing TMB_2 thin films as well as to deepen current understanding of how Al-addition influences the microstructure and performance under application-relevant conditions.

Here, we deposit AlB_2 thin films and show that especially their phase-constitution strongly depends on the Ar pressure used during non-reactive sputtering of an AlB_2 compound target. The observed phase formation is discussed with respect to *ab initio* calculations. The films' mechanical properties and microstructure are studied by nano-indentation and electron microscopes. Thermal stability investigations are conducted by in-situ X-ray diffraction during annealing to 1200 °C either in vacuum or lab-air.

2. Methods

2.1. Experimental setup

To synthesize AlB_x thin films, we used a high vacuum magnetron sputtering system with a base pressure below 10^{-4} Pa, a 2-inch AlB_2 target (Plansee Composite Materials GmbH) out of four magnetrons, a target-to-substrate distance ($d_{t\text{-}s}$) of 10 cm, and a substrate temperature (T_s) of 700 °C (almost the highest deposition temperature of the deposition chamber). We used the deposition temperature of 700 °C as previous study shows that sputtering AlB_2 target at 500 °C leads to amorphous structure [23] and preliminary work reveals that deposition at 600 °C results in only small phase fraction of α-AlB_2. The AlB_2 target was direct-current sputtered using a constant power of 160 W, which corresponds to a power density of 7.9 W/cm^2, onto a rotating 2-inch sapphire (0001-oriented) substrate placed 10 cm from the target surface. The normals of magnetron and substrate holder have an angle of 20° to each other, as depicted in Fig. 1. The depositions were performed under Ar pressures (p_{Ar}, 99.9999 % purity) of 0.4, 0.8, and 1.2 Pa with floating bias for 5h.

The chemical composition of the films was quantified by inductively

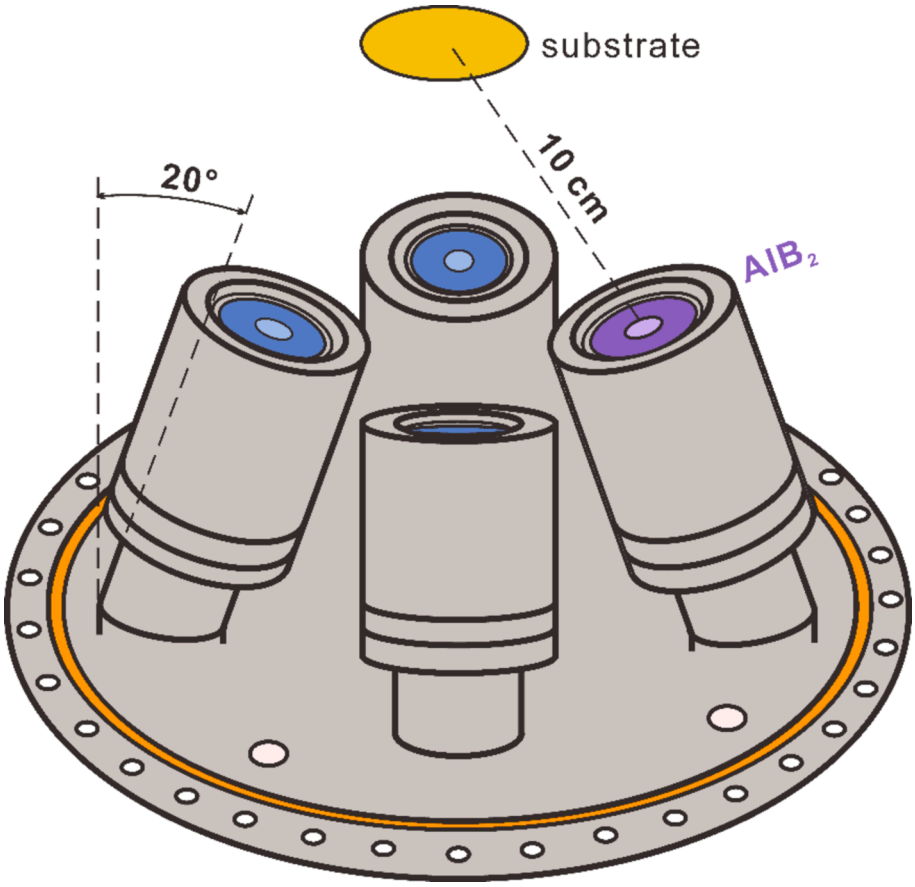

Fig. 1. Schematics of target-substrate arrangement for sputter deposition of AlB_x thin films.

coupled plasma optical emission spectroscopy (ICP-OES [36]) allowing accurate measurements for both B and metallic species [37]. For phase identification, a PANalytical X'Pert Pro X-ray diffraction (XRD) system and an Empyrean diffractometer with a Cu-Kα source (wavelength = 1.54 Å), powered with 45 kV and 40 mA, were utilized in the Bragg-Brentano and grazing-incidence geometries. Cross-sectional morphologies were investigated with a field emission scanning electron microscope (FE-SEM, Zeiss Supra 55) at an acceleration voltage of 3 kV.

Detailed microstructural investigations and chemical analysis were conducted for a selected sample, $AlB_{2.27}$, with a transmission electron microscope, TEM (FEI TECNAI F20). The $AlB_{2.27}$ sample was selected from the three different AlB_x thin films due to its simple phase constitution, revealed by XRD (next paragraph) results. The TEM was operated at 200 kV either in bright field or high-angle annular dark-field scanning TEM (HAADF-STEM) mode with an attached electron energy loss spectrometer (EELS). The TEM transparent sample was obtained by a standard lift-out procedure using a dual-beam ThermoFisher Scios 2 focused ion beam (FIB) system. Thermal stability and oxidation resistance of the selected $AlB_{2.27}$ thin film were studied by in-situ XRD with a PANalytical X'Pert Pro MPD diffractometer. Two $AlB_{2.27}$ samples were heated in a high-temperature furnace chamber (HTK 1200N) either in vacuum environment (10^{-2} Pa) or lab-air at ambient pressure (0.4 l/min flow rate). The in-situ XRD measurements were performed at 25 °C (as-deposited, as well as after the cooling following the annealing process) and between 400 and 1200 °C with a step of 50 °C. The samples were heated at a rate of 60 K/min to the desired temperature followed by a diffraction measurement for ~36 min at each step.

Indentation hardness (H) and Young's modulus (E) were assessed by nanoindentation (Ultra Micro Indentation System, UMIS) with a Berkovich diamond tip (Poisson's ratio $\nu = 0.07$; $E = 1141$ GPa) following the Oliver and Pharr method [38]. For each sample, we conducted 30 indents with loads 3–15 mN and analyzed their load–displacement curves (using $\nu = 0.25$ based on our DFT calculations and literature [21]). The E was obtained following the procedure and Eq. (2) in Ref. [39].

To estimate the effect of T_s and p_{Ar} on gas-phase transport of the sputtered Al and B species, we calculated the mean free path (λ, MFP) of Al and B atoms via [40]:

$$\lambda = \frac{kT_s}{p_{Ar}} \frac{1}{\pi\left(r_{Ar} + r_{Al,B}\right)^2 \sqrt{1 + \frac{m_{Al,B}}{m_{Ar}}}} \quad (1)$$

where k is Boltzmann's constant; m is the atomic mass ($m_B = 10.81$ amu, $m_{Al} = 26.98$ amu, and $m_{Ar} = 39.95$ amu), and r is the atomic radius ($r_B = 0.88$ Å, $r_{Al} = 1.26$ Å, and $r_{Ar} = 0.71$ Å).

2.2. Calculational details

DFT calculations were actualized using the Vienna Ab initio Simulation Package (VASP) [41] together with the Projector Augmented Wave (PAW) method [42] and the Perdew-Burke-Ernzerhof approximation for exchange–correlation effects [43]. The plane-wave cutoff energy was 600 eV and the Γ-centered k-point mesh was built with a length parameter of 60 Å. To model Al-substoichiometric $Al_{1-\delta}B_2$, Al vacancies were introduced on the metal sublattice of a 108-atom α-AlB_2 supercell following the Special Quasirandom Structure (SQS) method [44]. All structures were fully relaxed until forces on ions did not exceed 0.005 eV/Å. The corresponding formation energies, E_f, were evaluated with respect to the reference face-centered cubic (fcc-) Al and trigonal (trig-) B, consistent with our previous study [22]. Elastic constants of α-AlB_2 were calculated using the stress–strain method [45–47]. The polycrystalline Young's modulus, E, was calculated as $E = 9BG/(3B + G)$, where B and G represent the polycrystalline bulk and shear modulus, respectively, obtained following standard formulas (see e.g. Ref. [48]).

3. Results and discussion

3.1. Chemical compositions

Chemical analysis via ICP-OES of the films deposited with $p_{Ar} = 0.4$, 0.8, and 1.2 Pa reveals compositions of $AlB_{1.99}$, $AlB_{1.97}$, and $AlB_{2.27}$, respectively. Film compositions are determined by the arrival and loss fluxes of film-forming species. Our previous study [22] reveals that the heavier Al atoms are preferentially sputtered under higher angles while B are preferentially sputtered along the target normal. Sole consideration of the angular distribution of Al and B atoms would suggest B over-stoichiometric AlB_x films. Nevertheless, the substrate is at 10 cm and not fully at the axis of the magnetron, see Fig. 1. This might slightly reduce the (expected) B over-stoichiometry. The synthesized close-to-stoichiometric $AlB_{1.99}$ and $AlB_{1.97}$ thin films point toward preferential re-sputtering of B over Al from the Ar ions correlated with floating bias. The corresponding mean free path values for Al and B are $\lambda_{Al}^{0.4Pa} = 21.3$ cm, $\lambda_{Al}^{0.8Pa} = 10.6$ cm, $\lambda_B^{0.4Pa} = 37.5$ cm, $\lambda_B^{0.8Pa} = 18.8$ cm, which exceed the $d_{t\text{-}s}$ of 10 cm, and hence the gas phase scattering will be minor. However, increasing p_{Ar} to 1.2 Pa decreases λ_{Al} below 10 cm, whereas λ_B remains above ($\lambda_{Al}^{1.2Pa} = 7.1$ cm and $\lambda_B^{1.2Pa} = 12.5$ cm), indicating that gas scattering becomes relevant for Al but not for B. This suggests that the boron over-stoichiometry of $AlB_{2.27}$ is caused by preferential gas scattering of Al with increasing p_{Ar}. Other factors, including target-substrate distance, ionization degree [5], target potential [12] and substrate bias [49] can also influence the film stoichiometry, but are not discussed here as they are kept constant for the three films.

3.2. Microstructure

Bragg-Brentano X-ray diffractograms of the AlB_x films, Fig. 2, reveal signals of α-AlB_2, tetragonal (t-) AlB_{12}, and fcc-Al for the sample $AlB_{1.99}$, while fcc-Al is absent in the $AlB_{1.97}$ and $AlB_{2.27}$ samples. The $AlB_{2.27}$ thin film exhibits a very pronounced (0001)-orientation growth, see the strong (0001) and (0002) peaks, and even the (0003) can be detected. Additional grazing-incidence XRD data (Fig. 3) indicate that fcc-Al is only present at the substrate-film interface in $AlB_{1.99}$, and t-AlB_{12} is also only present at the substrate-film interface in $AlB_{2.27}$. The presence of t-AlB_{12} at the substrate-film interface in $AlB_{2.27}$ can be rationalized by the close-to-zero energy of formation of α-AlB_2 (revealed by literature [28] as well as our DFT calculations in Table 1) and the high substrate temperature of 700 °C, for which Al can easily vaporize, leading to the formation of t-AlB_{12}. Contrarily, grazing-incidence XRD shows that t-AlB_{12} is present within the $AlB_{1.99}$ and $AlB_{1.97}$ samples not just at the interface to the sapphire substrate (see following discussions).

The full width at half maximum (FWHM) of the (0001) peak is 0.280°, 0.337°, and 0.228° for $AlB_{1.99}$, $AlB_{1.97}$, and $AlB_{2.27}$, hinting towards larger and less-defected α-AlB_2 grains for $AlB_{2.27}$. Structural parameters of the films are derived using cell refinements of the XRD peaks. Aligned with the (0001) peak, the calculated c lattice parameters are 3.247 Å ($AlB_{1.99}$), 3.237 Å ($AlB_{1.97}$), and 3.248 Å ($AlB_{2.27}$). This is close to reference values of the stoichiometric α-AlB_2: $c = 3.253$ Å (ICDD 0039–1483, P6/mmm 191) and $c = 3.226$ Å (Table 1). For the a lattice parameter—aligned with the (10–11) peak—we obtain 2.972 Å ($AlB_{1.99}$) and 2.991 Å ($AlB_{1.97}$), which is 1.1 and 2.0 % below the reference values: $a = 3.005$ Å (ICDD standard) and $a = 3.033$ Å (Table 1). Obtaining a from the $AlB_{2.27}$ film is not possible as the XRD pattern exhibits only the (0001), (0002), and (0003) peaks but we later derive it from selective area electron diffraction (SAED) during TEM investigations.

According to the Al-B phase diagram, the AlB_2 line compound decomposes into AlB_{12} and Al at 956 ± 5 °C [33]. As there is no lower-B-containing phase, AlB_2 co-exists with Al for lower B contents than 66 at. % (below 659.7 °C with solid Al and above with liquid). Finite-temperature lattice dynamics calculations by Johansson et al. [28] predicted narrow chemical stability range of α-AlB_2 by considering B vacancies ($AlB_{2-\delta}$) or Al vacancies ($Al_{1-\delta}B_2$). For $0.073 \leq \delta \leq 0.096$, Al_{1-}

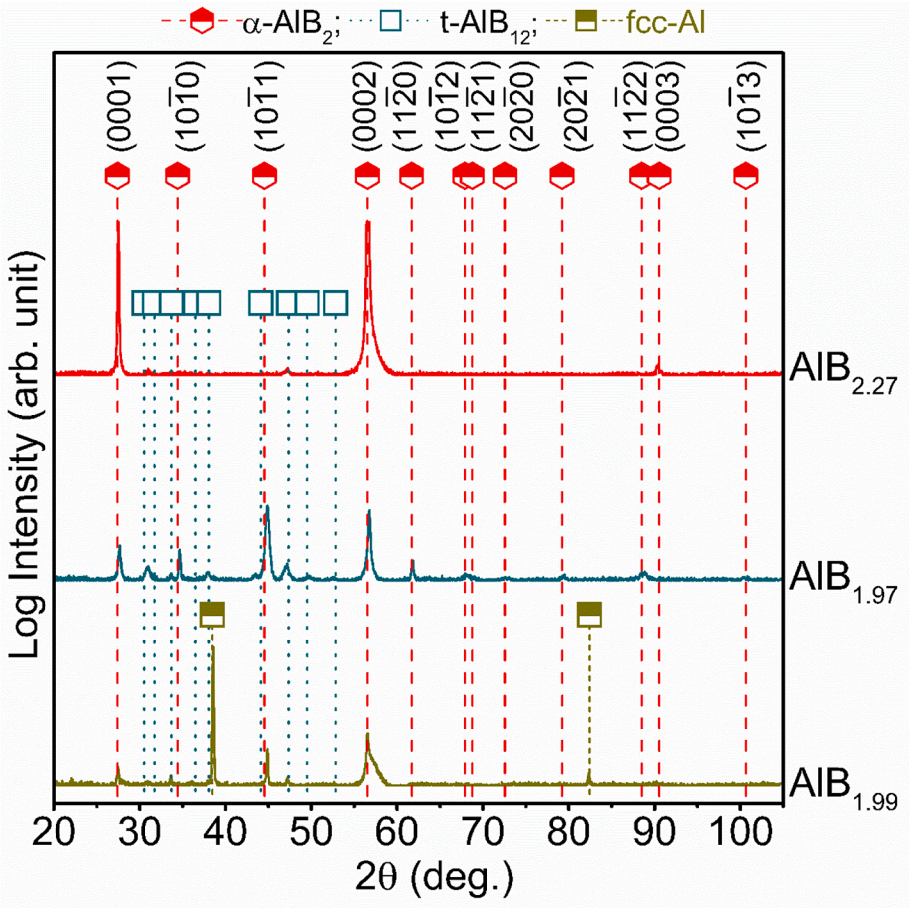

Fig. 2. Bragg-Brentano XRD patterns of AlB_x thin films deposited at 700 °C and different Ar pressures (p_{Ar} = 0.4, 0.8, 1.2 Pa). Standard peak positions for the α-type hexagonal phase (h-) AlB_2 (ICDD 0039–1483, P6/mmm 191), fcc-Al (ICDD0004-0478), and t-AlB_{12} (ICDD0012-0640) are marked by half-filled red hexagons, half-filled, and empty squares, respectively. (For interpretation of the references to colour in this figure legend, the reader is referred to the web version of this article.)

$_{\delta}B_2$ is predicted to be energetically favored over the perfect stoichiometric AlB_2, while outside this range (corresponding to $2.157 \leq x \leq 2.212$ for AlB_x), it consists of either additional Al-containing phases ($x < 2.157$) or α-B ($x > 2.212$) of different structures together with $Al_{1-\delta}B_2$ [28]. Thus, the formation of fcc-Al and t-AlB_{12}—seen experimentally in Fig. 2—can be interpreted by the narrow composition range of α-AlB_2. Yet, Al-substoichiometric structures modeled in Ref. [28] with B/Al ratios of ≤ 2.5 are far from the experimentally observed t-AlB_{12}. To estimate formation energies of "extremely" Al-substoichiometric structures, we employ DFT calculations to relax series of tetragonal-like α-$Al_{1-\delta}B_2$ supercells with δ between 0.92 and 0.5, yielding B/Al ratios of 4–25 (covering also AlB_{12}). The data is presented in Suppl. Tab. S1. While the formation energy differences between $Al_{1-\delta}B_2$ and the stoichiometric α-AlB_2 are large at 0 K (0.27–0.31 eV/at.), they gradually diminish at finite temperatures (by ~40 % at 1200 K) when accounting for configuration entropy contributions. At 956 ± 5 °C (~1229 K), where AlB_2 decomposes into AlB_{12} and Al, our DFT-predicted energy difference between α-AlB_2 and t-AlB_{12} is ~0.17 eV/at. (similar to the 0.18 eV/at. difference between the metastable cubic and the ground-state wurtzite AlN [50]), which can be overcome through lattice vibration effects. Hence, in line with the phase diagram, our DFT predictions indicate that decomposition of AlB_2 into an "extremely" Al-substoichiometric phase, such as t-AlB_{12}, requires very high temperatures.

From fracture cross-sections (Fig. 4), AlB_x thin films manifest phase-constitution dependent growth morphologies. The $AlB_{1.99}$ (Fig. 4a) reveals featureless morphology, in agreement with the broaden XRD peaks of α-AlB_2. The decomposition products t-AlB_{12} and fcc-Al compete with the forming α-AlB_2, leading to ultra fine grains. The $AlB_{1.97}$ (Fig. 4b) presents larger grains, which can be rationalized by the decomposition of α-AlB_2 suggested by lower diffraction intensity of fcc-Al compared with $AlB_{1.99}$ (Fig. 2). The $AlB_{2.27}$ (Fig. 4c) shows fiber-like growth morphology. The thicknesses of the $AlB_{1.99}$, $AlB_{1.97}$, $AlB_{2.27}$ films are 1.71, 1.66, 1.44 μm, corresponding to growth rates of 5.7, 5.3, and 4.8 nm/min, respectively. The growth rate decreases with increasing working gas pressure owing to the increasing collisions among the sputtered species and Ar.

The $AlB_{2.27}$ thin film was selected for further detailed TEM investigations for its highest phase purity and to identify where the surplus B is located. One possibility, according to Ref. [28] for over-stoichiometric AlB_x ($x > 2.215$), would be the segregation as crystalline α-B. The TEM bright-field (BF) image shows large grains (diameter > 1 μm), coinciding with the sharp XRD peaks in Fig. 2, with platelet-like bright segregations (~10–60 nm width) parallel to the substrate-film interface, Fig. 5a. As displayed in the inserted SAED pattern of the region A (marked by a white circle in Fig. 5a), the film reveals only one crystalline structure, that of α-AlB_2. The discrete diffraction spots convey high crystalline quality. As the columnar grains are larger in length and diameter than the aperture size (and sample thickness), a single-crystal pattern is obtained. Analysis of the diffraction spots reveals lattice parameters of a = 2.999 Å and c = 3.248 Å (c/a ratio of 1.083), in accordance with the XRD data. The bright regions in the BF image, repeatably present (as platelet-like features parallel to the substrate surface) within the α-AlB_2 grain are purely boron, as confirmed by the EELS linescan 1, see the indicated place of the linescan (across ~200 nm length) STEM-HADDF image Fig. 5b. The region used for this STEM-HADDF image (in which these platelet-like features are dark, indicating

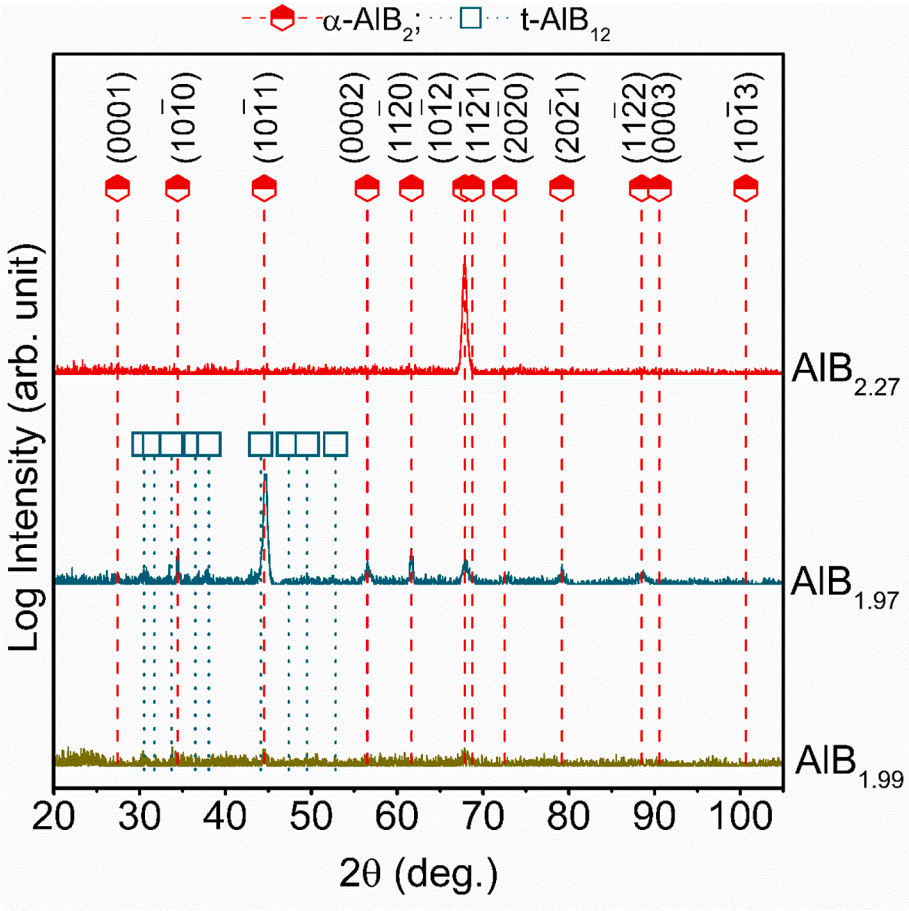

Fig. 3. Grazing-incidence XRD patterns of AlB_x (x = 1.99, 1.97, 2.27) thin films deposited at 700 °C and different Ar pressures (p_{Ar} = 0.4, 0.8, 1.2 Pa). Standard peak positions for the α-type hexagonal phase (h-) AlB_2 (ICDD 0039–1483, P6/mmm 191), and t-AlB_{12} (ICDD0012-0640) are marked by half-filled red hexagons, half-filled, and empty squares, respectively. (For interpretation of the references to colour in this figure legend, the reader is referred to the web version of this article.)

Table 1
Ab initio calculated formation energies, E_f (in eV./at.), lattice parameters, *a, c* (in Å), elastic constants, C_{ij} (in GPa), polycrystalline bulk, shear, and Young's moduli, *B*, *G*, and *E* (all in GPa), directional Young's moduli and Cauchy pressures, $E_{[hkil]}$ and $CP_{[hkil]}$ (in GPa) of perfect defect-free α-AlB_2 (P6/mmm).

Source	E_f	*a*	*c*	C_{11}	C_{33}	C_{12}	C_{13}	C_{44}	*B*	*G*	*E*	$E_{[-12-10]}$	$E_{[0001]}$	*ν*	*G/B*
Our work	−0.052	3.033	3.226	552	432	92	0	45	188	124	305	536	432	0.23	0.66
Mat. Proj. [30]	−0.050	2.99	3.26	578	400	114	−3	69	190	145	347	556	400	0.20	0.76
Ref. [27]	–	2.983	3.006	522	255	75	79	32	186	96	245	492	234	0.28	0.51
Ref. [29]	–	3.008	3.261	665	417	41	17	58	205	154	369	662	416	0.2	0.75

lower mass) is marked with a white-dashed rectangular area in Fig. 5a (labelled with b). The high-resolution TEM (HRTEM) examination of a region comprising the B-platelets and the AlB_2 grain (labelled c in Fig. 5a) proves that the B regions are amorphous, see Fig. 5c and the Fast Fourier Transformation (FFT) of a region within this platelet (labelled B in Fig. 5c). This is consistent with XRD and SAED, which showed that α-AlB_2 was the only crystalline phase identified. Thus, different from previous DFT calculations [28], which suggested α-AlB_2 and α-B for AlB_x with $x > 2.215$, we observe the formation of α-AlB_2 crystals and amorphous boron in the as deposited $AlB_{2.27}$ thin film. Inverse FFT studies (IFFT) of the crystalline AlB_2 region (labelled C in Fig. 5c) indicate the presence of many stacking faults, marked by arrows. The energetically favored formation of stacking faults is in line with the close-to-zero formation energy of α-AlB_2 (−0.052 eV/at. from our DFT calculations). The EELS linescan 2 (across the substrate-film interface and a smaller B-platelet), Fig. 5b, again proves the 100 at% B content of the dark-appearing regions (within the STEM-HADDF image) and a lower B content close to the sapphire substrate. The EELS linescan 3, which does not run across such a dark platelet-like region but slightly brighter regions close to the substrate (Fig. 5b), has no increased B signal but indicates a lower B content at these brighter regions. The latter is in line with the combined XRD and GIXRD studies of this film, which showed that t-AlB_{12} is only present at the interface to the sapphire. Formation of such a B-rich phase would require the presence of Al-rich regions with the $AlB_{2.27}$ thin film. An HRTEM study of such a film-substrate interface region, labelled with d in Fig. 5a, shows no other phase than α-AlB_2 (Fig. 5d). The different contrasts within this image are essentially due to different orientations (as suggested by FFT studies).

3.3. Mechanical properties

The $AlB_{1.99}$, $AlB_{1.97}$, and $AlB_{2.27}$ thin films show *H* values of 17.3 ± 0.9, 14.5 ± 1.4, and 19.2 ± 1.2 GPa, respectively. Compared to other binary diboride thin films like TiB_x (22–44 GPa) [6,51,52], WB_x (25–40 GPa) [15], TaB_x (27–43 GPa) [12], $HfB_{2.7}$ (44 GPa) [53], $CrB_{1.94}$ (23.5 GPa) [54], the *H* of our AlB_x thin films is lower. However, the measured

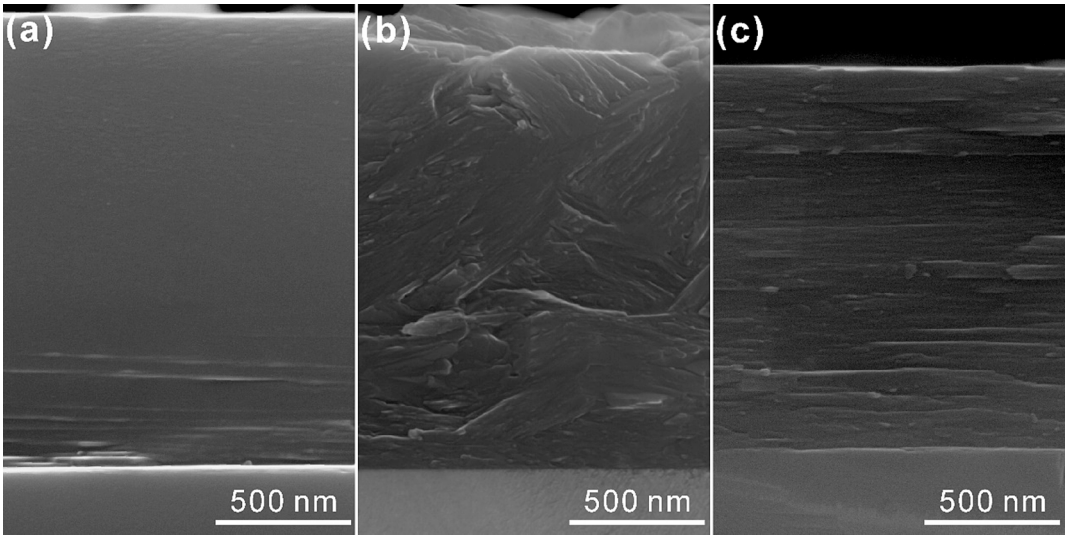

Fig. 4. SEM cross sectional images of AlB_x thin films deposited at different argon pressures at 700 °C: (a) x = 1.99 (0.4 Pa), (b) 1.97 (0.8 Pa), (c) 2.27 (1.2 Pa).

low hardness of AlB_x thin films could nicely explain the significantly reduced *H* of Al-containing ternary TMB_2s in comparison with their binary counterparts. Our previous study [22] also shows a decline of *H* with Al-addition to TaB_x, where $TaB_{1.64}$ exhibits an *H* of 38.8 ± 1.4 GPa comparing with the 31.3 ± 1.0 GPa of $(Ta_{0.52}Al_{0.48})B_{2.29}$. Hahn et al. [23] observed a sharp decline of *H* from the 42 ± 2 GPa of $WB_{1.86}$ to the 24 ± 1 GPa of $(W_{0.50}Al_{0.50})B_{1.90}$. Kashani et al. [55] reported close *H* values of $(Ti_{0.55}Al_{0.45})B_{2.03}$ (19 ± 2 GPa) and $(Ti_{0.36}Al_{0.64})B_{2.03}$ (19 ± 2 GPa) as $AlB_{2.27}$ thin film in this study, and even $(Ti_{0.15}Al_{0.85})B_{2.03}$ with a lower *H* of 12 ± 1 GPa.

Generally, grain size [56], orientation anisotropy [6,8,15,57], and film stoichiometry [58,59] are crucial factors for the *H* values of TMB_2s. Correlated with the Hall-Petch relation, the *H* of nanocrystalline materials increases with decreasing grain size [56]. Especially due to the large anisotropy of the hexagonal AlB_2-type crystal, a pronounced orientation-relation of *H* was reported for several diboride thin films [6,8,15,57]. For example, *H* increased by > 10 GPa and > 15 GPa for TiB_x [6] and WB_x [15], respectively, with increasing (0001) orientation. Hardness values even above 40 GPa were obtained by highly (0001)-oriented TaB_2 (45.9 GPa) [57] and (0001)-oriented ZrB_2 (45.0 GPa) [8]. Furthermore, slightly overstoichiometric diboride thin films regularly provide higher *H* than their stoichiometric counterparts due to the formed B-rich tissue phases, which hinders dislocation gliding across column boundaries [58,59]. Contrarily, $AlB_{2.27}$ exhibits large grains (with diameters above 1 μm) and the excess B causes the formation of B-platelets perpendicular to the growth direction. Therefore, the hardness value of the $AlB_{2.27}$ thin film is more in line with those of the bulk counterparts of diborides, which are frequently close to 20 GPa (e.g., *H* of TiB_2 bulk is 24 ± 2 GPa [60]). The other two thin films, $AlB_{1.97}$ and $AlB_{1.99}$, although rather close to stoichiometry, do exhibit a pronounced content of other phases, especially the soft fcc-Al for $AlB_{1.99}$ explaining their comparably lower average *H* values compared to the over-stoichiometric sample.

The cohesive energy chiefly determines the *E* modulus of materials [61], but as very small grained materials often have lower *E* due to the noticeable contribution from the boundaries [62], any comparison should consider this. Additionally, any pronounced anisotropy like for diborides [63] and off-stoichiometry [17,64] can influence the *E* modulus. Furthermore, it is reasonable to assume that the stress state of the as deposited films affects the elastic modulus [65].

Among the three AlB_2-based films, $AlB_{1.99}$ (deposited at 0.4 Pa) has the lowest *E* of 289.3 ± 8.4 GPa. The film has no pronounced growth orientation and despite the noticeable phase contribution of fcc-Al to α-AlB_2, the value is comparable to the DFT polycrystalline Young's modulus for α-AlB_2, *E* = 305 GPa (see Table 1). The $AlB_{1.97}$ film, which exhibits a more (10–11) and (0001) oriented growth of α-AlB_2 with a much smaller contribution from fcc-Al but an increased contribution from t-AlB_{12}, exhibits the highest *E* value of 353 ± 19.7 GPa among the three AlB_2-based films. The corresponding DFT values for α-AlB_2 are: $E_{[-12-10]} = E_{[10-10]}$ = 536 GPa, $E_{[0001]}$ = 432 GPa (see Table 1). Thus, the additional strong contributions of (0001)-oriented grains next to the massively reduced contribution form fcc-Al could account for the higher *E* modulus. The $AlB_{2.27}$ thin film deposited at 1.2 Pa, showing pronounced (0001)-oriented α-AlB_2 grains next to amorphous B, exhibits 331.8 ± 14.4 GPa. The rather coarse α-AlB_2 grains (larger than the coating thickness) should be suitable for a comparison with the $E_{[0001]}$ = 432 GPa obtained by our DFT. The deviation may be (partially) attributed to the amorphous B phase (consistently with Ref. [17,64]) as well as many stacking faults within the α-AlB_2 grains, see Fig. 2c. Note that elastic constants, thus, Young's moduli significantly vary among DFT studies (see Table 1). This is likely related to the low chemical stability of α-AlB_2 (close-to-zero formation energy, see Table 1), making elastic constants sensitive to the chosen computational approach (e.g., the magnitude of the applied strain in the stress/strain method, here 1.9 %; the convergence criteria during relaxation etc.).

3.4. Thermal stability and oxidation resistance

The $AlB_{2.27}$ thin film was further studied in detail for its thermal stability by vacuum-annealing up to 1200 °C by in-situ XRD measurements, as shown in Fig. 6. By increasing the temperature from RT to 950 °C, the diffraction peaks of α-AlB_2 continuously shift to lower 2θ angles. The peaks from the (0001) and (0002) planes shift from 27.49° to 27.03° and 56.62° to 55.57° upon increasing the temperature from RT to 950 °C, respectively. Correspondingly, the lattice constant *c* exhibits a linear increase from RT to 950 °C, which can be fitted to the following expression:

$$c = 3.22985 + 5.45585 \times 10^{-5}\, T\ (\text{Å}) \quad (2)$$

where 298.15 K ≤ *T* ≤ 1248.15 K. From the fitted equation, the thermal expansion coefficient at 298.15 K is $\alpha_c\,(298) = 16.80 \times 10^{-6}\ K^{-1}$, which is close to the theoretical value of $12.58 \times 10^{-6}\ K^{-1}$ from Ref. [28]. The t-AlB_{12} diffraction signals appear upon annealing the film at 900 °C, suggesting that between 850 and 900 °C, the $AlB_{2.27}$ film starts to decompose. The decomposition temperature is lower than the decomposition temperature (956 ± 5 °C) based on the Al-B phase diagram

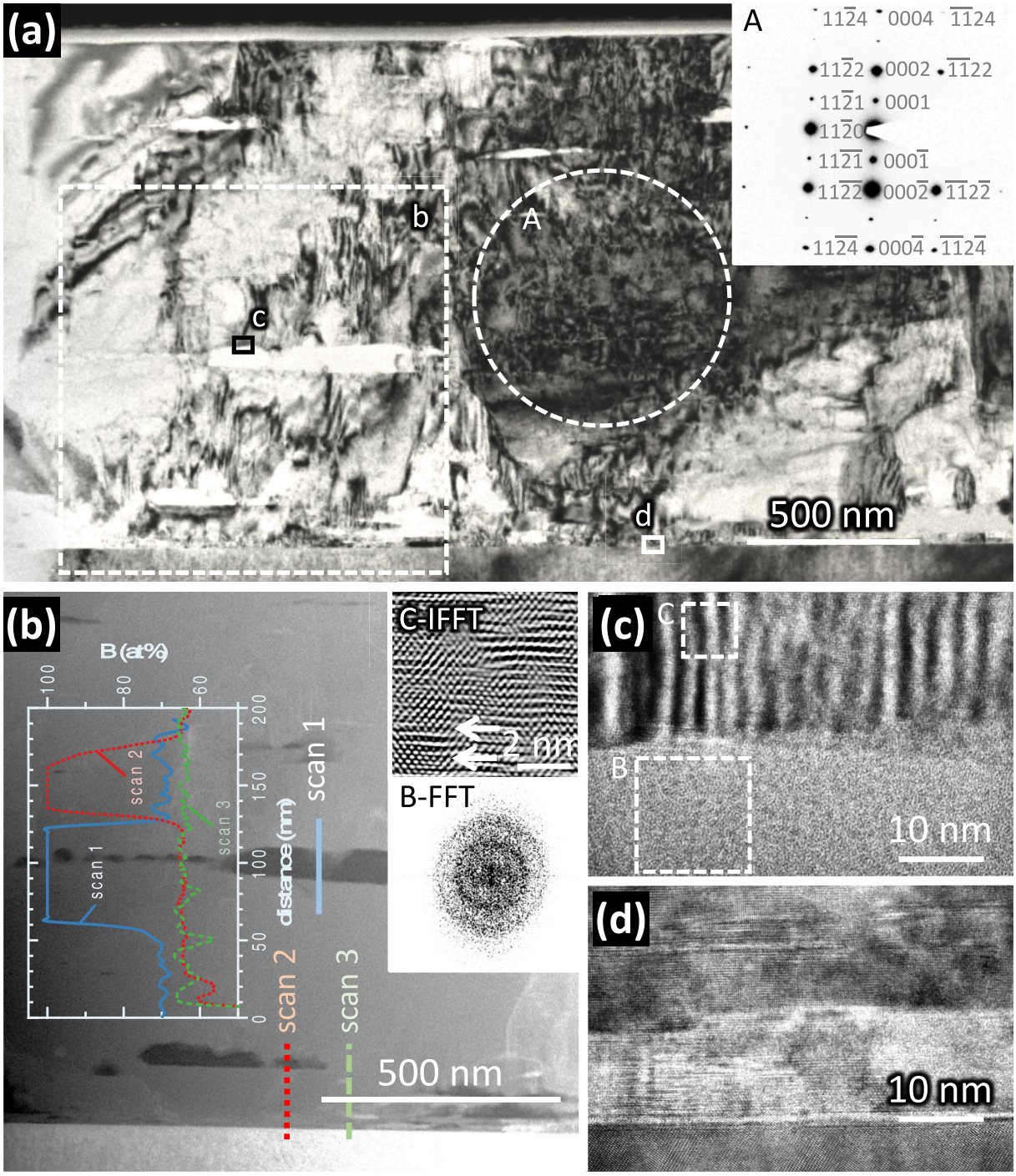

Fig. 5. TEM investigations of $AlB_{2.27}$ thin film: (a) Cross-sectional BF TEM image with SAED pattern of the circled A region as inset, (b) STEM-HADDF image with EELS linescan profiles from three different regions (as marked with the scan 1, 2, and 3), FFT of region B from (c) and IFFT of region C (the arrows mark stacking faults) from (c) as insets, (c) HRTEM image of the region marked with c in (a) covering a B-platelet and AlB_2 grain, (d) HRTEM image of the region marked with d in (a) covering the interface between the film and the sapphire substrate.

[33], which can be explained by the B-overstoichiometry of $AlB_{2.27}$, enabling the formation of t-AlB_{12} at a lower temperature than in stoichiometric AlB_2. Tetragonal AlB_{12} is also observed as the decomposition product of $(Ti_{0.36}Al_{0.64})B_{2.03}$ thin film after vacuum annealing at 1000 °C for 3 h, verified by atom probe tomography (APT) and SAED [66]. Aluminum, the other decomposition product, is not detectable by XRD at this temperature, due to its molten state (melting point of Al is ~660 °C [67], which can be lower at vacuum pressure). At 1000 °C, the h-AlB_{10} phase is present as another decomposition product. Meanwhile, the original peaks of the α-AlB_2 phase are absent conveying its complete decomposition at 1000 °C, which is confined as the application temperature limit of Al-rich $(Ti_{0.36}Al_{0.64})B_{2.03}$ thin film in vacuum [66]. The h-AlB_{10} phase is hexagonal-structured with a of 7.835 and c of 15.910 Å, and was found after a long-time (> 5h) annealing (at $T = 1350–1400$ °C) of an amorphous film prepared by thermal evaporation of B and Al_2O_3 mixture and deposited onto glass or sapphire substrates (T = 300–400 °C) [68]. A more recent study pointed out that h-AlB_{10} is a high-temperature compound from the reaction among Al and B and typically forms at $T > 1000$ °C [69]. Considering the excess boron within the $AlB_{2.27}$ thin film and metallic Al from the thermal decomposition of

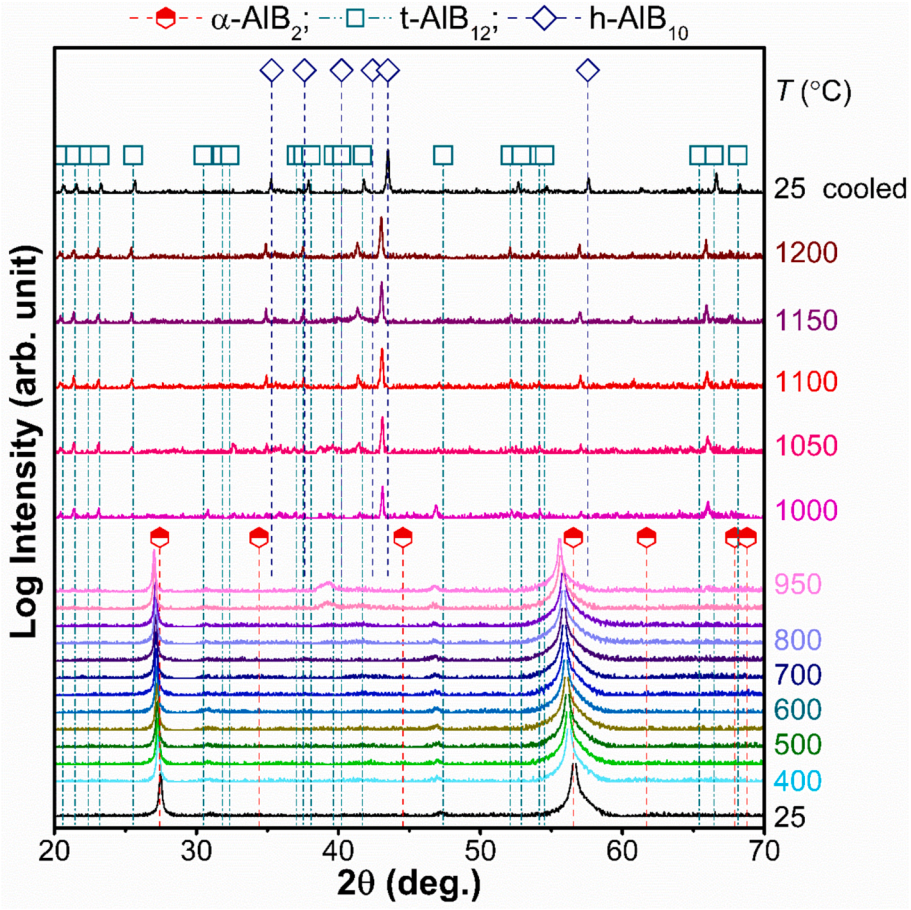

Fig. 6. In-situ X-ray diffraction patterns recorded during annealing in vacuum up to 1200 °C of an $AlB_{2.27}$ thin film deposited on a sapphire substrate. The sample temperature corresponding to each diffraction experiment is labeled on the right end of the patterns. The standard peak positions for the α-type h-AlB_2 (ICDD 0039-1483, P6/mmm 191) are indicated with half-filled red hexagons. The standard peak positions for t-AlB_{12} (ICDD0012-0640) and h-AlB_{10} (ICDD0022-0002) are marked with empty horizontally and 45° tiled squares. (For interpretation of the references to colour in this figure legend, the reader is referred to the web version of this article.)

α-AlB_2 [70], the formation of h-AlB_{10} at 1000 °C is reasonable. While there are also some reports on the orthorhombic (o-) structured AlB_{10} phase with *a* of 8.881 Å, *b* of 9.100 Å, and *c* of 5.680 [71] or 5.690 Å [72]. The AlB_{10} phase, irrespective of crystal structure, is not described in the Al-B phase diagram [33,70,73]. The formation of h-AlB_{10} could be ascribed to the non-equilibrium state at the thermal treatment in this study. Nevertheless, to fully ascertain the temperature- and/or time-induced phase transformation of Al-B system, further TEM or APT observations would be needed. Elevating *T* from 1000 to 1200 °C results in nearly no further change of the phase constitution, except for the continuous shift of the diffraction peaks of t-AlB_{12} and h-AlB_{10} to lower 2θ angles. After cooling down to 25 °C, the t-AlB_{12} and h-AlB_{10} peaks are closer to the standard positions (thus, they shifted to larger diffraction angles).

In-situ XRD studies were also performed during lab-air annealing of the $AlB_{2.27}$ thin films up to 1200 °C to reveal their oxidation sequence, Fig. 7. The $AlB_{2.27}$ thin film demonstrates an unaltered structure up to 950 °C. Similar to vacuum-annealing, the (0001) and (0002) peaks continuously move to lower 2θ angles with *T* increasing from RT to 950 °C, shifting by 0.48° and 1.10°, respectively. The linearly increasing lattice constant *c* is fitted into the following expression:

$$c = 3.22359 + 6.03679 \times 10^{-5}\, T\ (\text{Å}) \tag{3}$$

where 298.15 K ≤ *T* ≤ 1248.15 K. Correspondingly, the thermal expansion coefficient at 298.15 K obtained here is $\alpha_c(298) = 18.6 \times 10^{-6}\ K^{-1}$, which is close to the value of $16.80 \times 10^{-6}\ K^{-1}$ obtained during vacuum annealing. Notably, t-AlB_{12} is absent here in the non-annealed state and not even at any temperature up to the maximum of 900 °C, further conveying its local formation at the interface to sapphire substrate in the $AlB_{2.27}$ thin film. The postponed formation of the thermal decomposition product of t-AlB_{12} during oxidation compared with vacuum annealing can be ascribed to the suppressed Al evaporation by the protective Al-O layer on the sample surface at air atmosphere. At 1000 °C, α-Al_2O_3 and orthorhombic (o-) $Al_{18}B_4O_{33}$ ($9Al_2O_3{\cdot}2B_2O_3$ [74]), can be detected, suggesting their onset of formation between 950 and 1000 °C. The o-$Al_{18}B_4O_{33}$ is an equilibrium phase according to the phase diagram of ($Al_2O_3 + B_2O_3$) binary system [75]. It is formed as the reaction product of Al_2O_3 and B_2O_3 following the equation of

$$9Al_2O_3\ (s) + 2B_2O_3\ (l) = Al_{18}B_4O_{33}\ (s) \tag{4}$$

Their corresponding peaks gain intensity upon a further increase in *T* to 1100 °C. Compared with other binary boride thin films, the $AlB_{2.27}$ thin film shows an exceptional oxidation resistance with much higher onset oxidation temperature of 950–1000 °C. $ReB_{2.35}$, $TiB_{2.40}$, $TiB_{2.57}$, $WB_{1.88}$, $CrB_{1.94}$, $TaB_{1.53}$, and $HfB_{2.36}$ thin films exhibit oxidation onset temperatures of room temperature [24], ~400 °C [16], ~490 °C [76], ~500 °C [36], ~600 °C [54], ~620 °C [36] and ~800 °C [36], respectively. $ReB_{2.35}$ thin film already forms $HReO_4$ after exposure to air for two days [24]. While for other binary boride thin films including $TiB_{2.40}$, $TiB_{2.57}$, $WB_{1.88}$, $CrB_{1.94}$, $TaB_{1.53}$, and $HfB_{2.36}$ [16,36,54,76], above their onset temperatures for oxidation the mass increases till full oxidation. Subsequently, the mass decreases and the oxide scales

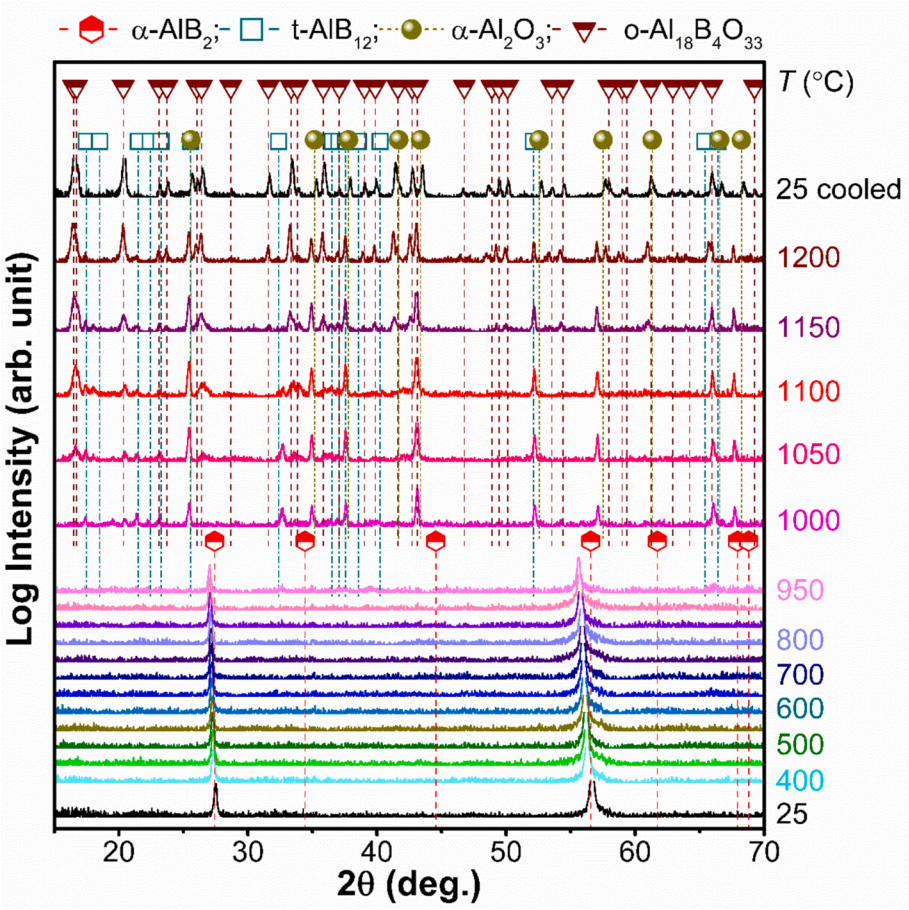

Fig. 7. In-situ X-ray diffraction patterns recorded during oxidation in lab-air up to 1200 °C of the $AlB_{2.27}$ thin film deposited on sapphire substrate. The sample temperature corresponding to each diffraction experiment is given on the right end of the patterns. The standard peak positions for the α-type h-AlB_2 (ICDD 0039-1483, P6/mmm 191) are indicated with half-filled red hexagons. The standard peak positions for t-AlB_{12} (ICDD0012-0640) are marked with empty squares. The yellow full-filled circles and purple half-filled triangle indicate the positions of the oxides hexagonal α-Al_2O_3 (ICDD0046-1212) and orthorhombic (o-) $Al_{18}B_4O_{33}$ (ICDD0032-0003). (For interpretation of the references to colour in this figure legend, the reader is referred to the web version of this article.)

become highly porous as a result of the evaporation of volatile B_2O_3 phase. The exceptional oxidation resistance of $AlB_{2.27}$ thin film compared with other binary borides can be explained by the reaction between B_2O_3 and Al_2O_3, which suppresses the evaporation of B_2O_3. Increasing T from 1100 to 1200 °C causes the o-$Al_{18}B_4O_{33}$ peaks to have decreased full width at half maximum with increased intensity, which is a typical sign for grain growth. Contrarily, the shape and intensity of the α-Al_2O_3 peaks remain almost unchanged. The decomposition product t-AlB_{12} can be detected between 950 and 1200 °C with gradually decreasing intensity for increasing temperature. After cooling down to 25 °C, the XRD peaks of α-Al_2O_3 and o-$Al_{18}B_4O_{33}$ are closer to their standard positions. Thus, they shifted to larger diffraction angles from their 1200 °C data.

4. Conclusions

Despite representing the most common phase prototype of transition metal diborides and being widely used for alloying, very little experimental data exist on α-AlB_2 thin films, which can be related to its close-to-zero formation energy. Within this study, we showed that non-reactive sputtering of an AlB_2 compound target allows formation of a crystalline α-AlB_2 thin film. With increasing Ar pressure during deposition from p_{Ar} = 0.4 to 0.8 to 1.2 Pa—while keeping the substrate temperature at 700 °C—the chemistry of the AlB_x thin films slightly changes from x = 1.99 to 1.97 to 2.27, respectively. But more importantly, their phase composition changes from Al + AlB_{12} + AlB_2 (p_{Ar} = 0.4 Pa) to AlB_{12} + AlB_2 (p_{Ar} = 0.8 Pa)—with increasing AlB_2 phase fraction upon increasing p_{Ar}—to single-crystalline AlB_2 (p_{Ar} = 1.2 Pa, $AlB_{2.27}$). The structural complexity of AlB_x thin films nicely agree with the close-to-zero formation energy of α-AlB_2.

Detailed XRD studies reveal that the fcc-Al phase within the $AlB_{1.99}$ thin film is only present at the interface to the sapphire substrate. The phase constitution can be rationalized by previous *ab initio* calculations and those presented here, as well as by the high substrate temperature used during deposition. The $AlB_{2.27}$ thin film is composed of nearly stoichiometric large columnar α-AlB_2 grains (with highly 0001-growth-oriented columns spanning across the entire film thickness of ~1.4 μm and diameters above 1 μm) and platelet-like amorphous B regions. The α-AlB_2 crystals exhibit many stacking faults and the amorphous B platelets (with different sizes and thicknesses) are always arranged parallel to the substrate interface. The as deposited film has an indentation hardness of 19.2 ± 14.4 GPa and indentation modulus of 331.8 ± 14.4 GPa, which is in good agreement with the DFT-predicted value (305 GPa). The relatively low hardness of $AlB_{2.27}$ thin film compared with other binary boride thin films could account for the often observed decline in hardness induced by Al-addition into binary TMB_2.

In-situ XRD studies of the $AlB_{2.27}$ thin film during vacuum-annealing up to 1200 °C reveal that the film remains nearly unchanged (with the α-AlB_2 phase and no crystalline B) up to 850 °C. For T > 850 °C thermal decomposition of α-AlB_2 into AlB_{12} and with ≥ 1000 °C also AlB_{10} (plus Al, which is not detectable by XRD due to its molten state at this temperature) is present. A corresponding study in lab-air reveals that the

$AlB_{2.27}$ thin film starts to oxidize between 950 and 1000 °C by forming α-Al_2O_3 and o-$Al_{18}B_4O_{33}$. The exceptional oxidation resistance of $AlB_{2.27}$ thin film is explainedby the suppressed evaporation of B_2O_3 during oxidation by reaction with Al_2O_3, which is detrimental and conduces to porous oxide scale for other binary TMB_2 such as TiB_2, WB_2, CrB_2, TaB_2, and HfB_2. The results demonstrate that a controlled deposition process allows to prepare AlB_2 thin films with their AlB_2-prototype structure. The slightly overstoichiometric $AlB_{2.27}$ film demonstrates exceptional oxidation resistance compared to binary TMB_2s, which provides a solid basis for future research on Al-containing TMB_2s.

CRediT authorship contribution statement

Chun Hu: Writing – review & editing, Writing – original draft, Validation, Methodology, Investigation, Formal analysis, Data curation, Conceptualization. **Stanislav Mráz:** Writing – review & editing, Methodology, Conceptualization. **Peter J. Pöllmann:** Writing – review & editing, Methodology. **T. Wojcik:** Writing – review & editing, Investigation. **M. Podsednik:** Writing – review & editing, Investigation. **B. Hajas:** Writing – review & editing, Methodology. **A. Limbeck:** Writing – review & editing, Resources. **Nikola Koutná:** Writing – review & editing, Supervision, Software, Project administration. **Jochen M. Schneider:** Writing – review & editing, Supervision, Resources, Project administration, Funding acquisition. **Paul H. Mayrhofer:** Writing – review & editing, Supervision, Project administration, Funding acquisition.

Declaration of competing interest

The authors declare that they have no known competing financial interests or personal relationships that could have appeared to influence the work reported in this paper.

Acknowledgments

The authors thank the X-ray center (XRC) and the electron microscopy center (USTEM) of TU Wien for using their facilities. We acknowledge TU Wien Bibliothek for financial support through its Open Access Funding Program. PHM appreciates the support by Plansee SE. JMS gratefully acknowledges funding from the German Research Foundation (DFG SCHN735/42-1). NK is grateful to the support from the Austrian Science Fund (FWF; 10.55776/T1308). CH thanks the support from the State Scholarship Fund of China (No. 202006370042) during her PhD at TU Wien and the grants for diploma and PhD thesis (KUWI) during her research stay at Materials Chemistry, RWTH Aachen University. Computational resources were provided by the Vienna Scientific Cluster (VSC) and by the Swedish National Infrastructure for Computing (SNIC), partially funded by the Swedish Research Council through Grant Agreement Nr. VR-2015-04630, on the Clusters located at the National Supercomputer Centre (NSC) in Linköping, the Center for High Performance Computing (PDC) in Stockholm.

Appendix A. Supplementary data

Supplementary data to this article can be found online at https://doi.org/10.1016/j.matdes.2025.113584.

Data availability

Data will be made available on request.

References

[1] C. Mitterer, Borides in thin film technology, J. Solid State Chem. 133 (1) (1997) 279–291, https://doi.org/10.1006/jssc.1997.7456.
[2] W.G. Fahrenholtz, G.E. Hilmas, Ultra-high temperature ceramics: Materials for extreme environments, Scr. Mater. 129 (2017) 94–99, https://doi.org/10.1016/j.scriptamat.2016.10.018.
[3] M. Magnuson, L. Hultman, H. Högberg, Review of transition-metal diboride thin films, Vacuum 196 (2022) 110567, https://doi.org/10.1016/j.vacuum.2021.110567.
[4] N. Nedfors, D. Primetzhofer, I. Zhirkov, J. Palisaitis, P.O.Å. Persson, J.E. Greene, I. Petrov, J. Rosen, The influence of pressure and magnetic field on the deposition of epitaxial TiB_x thin films from DC magnetron sputtering, Vacuum 177 (2020) 109355, https://doi.org/10.1016/j.vacuum.2020.109355.
[5] N. Hellgren, J. Thörnberg, I. Zhirkov, M.A. Sortica, I. Petrov, J.E. Greene, L. Hultman, J. Rosen, High-power impulse magnetron sputter deposition of TiB_x thin films: Effects of pressure and growth temperature, Vacuum 169 (2019) 108884, https://doi.org/10.1016/j.vacuum.2019.108884.
[6] C. Fuger, R. Hahn, A. Hirle, P. Kutrowatz, M. Weiss, A. Limbeck, O. Hunold, P. Polcik, H. Riedl, Revisiting the origins of super-hardness in TiB_{2+z} thin films – Impact of growth conditions and anisotropy, Surf. Coat. Technol. 446 (2022) 128806, https://doi.org/10.1016/j.surfcoat.2022.128806.
[7] C. Schnitter, I. Petrov, I. Zhirkov, L. Hultman, J. Palisaitis, J. Rosen, H. Högberg, Effect of low-energy ion assistance on the properties of sputtered ZrB_2 films, Vacuum 195 (2022) 110688, https://doi.org/10.1016/j.vacuum.2021.110688.
[8] L. Tengdelius, E. Broitman, J. Lu, F. Eriksson, J. Birch, T. Nyberg, L. Hultman, H. Högberg, Hard and elastic epitaxial ZrB_2 thin films on Al_2O_3(0001) substrates deposited by magnetron sputtering from a ZrB_2 compound target, Acta Mater. 111 (2016) 166–172, https://doi.org/10.1016/j.actamat.2016.03.064.
[9] T. Glechner, O.E. Hudak, T. Wojcik, L. Haager, F. Bohrn, H. Hutter, O. Hunold, J. Ramm, S. Kolozsvári, E. Pitthan, D. Primetzhofer, H. Riedl, Influence of the non-metal species on the oxidation kinetics of Hf, HfN, HfC, and HfB_2 coatings, Mater. Des. 211 (2021) 110136, https://doi.org/10.1016/j.matdes.2021.110136.
[10] V. Moraes, L. Zauner, T. Wojcik, M. Arndt, P. Polcik, H. Riedl, P.H. Mayrhofer, Thermally stable superhard diborides: An ab initio guided case study for V-W-diboride thin films, Acta Mater. 186 (2020) 487–493, https://doi.org/10.1016/j.actamat.2020.01.014.
[11] N. Nedfors, O. Tengstrand, J. Lu, P. Eklund, P.O.Å. Persson, L. Hultman, U. Jansson, Superhard NbB_{2-x} thin films deposited by dc magnetron sputtering, Surf. Coat. Technol. 257 (2014) 295–300, https://doi.org/10.1016/j.surfcoat.2014.07.087.
[12] V. Šroba, T. Fiantok, M. Truchlý, T. Roch, M. Zahoran, B. Grančič, P. Švec, Š. Nagy, V. Izai, P. Kúš, M. Mikula, Structure evolution and mechanical properties of hard tantalum diboride films, J. Vac. Sci. Technol. A 38 (3) (2020) 033408, https://doi.org/10.1116/6.0000155.
[13] M.M. Dorri, J. Thörnberg, N. Hellgren, J. Palisaitis, A. Petruhins, F.F. Klimashin, L. Hultman, I. Petrov, P.O.Å. Persson, J. Rosen, Synthesis and characterization of CrB_2 thin films grown by DC magnetron sputtering, Scr. Mater. 200 (2021) 113915, https://doi.org/10.1016/j.scriptamat.2021.113915.
[14] P. Malinovskis, J. Palisaitis, P.O.Å. Persson, E. Lewin, U. Jansson, Synthesis and characterization of MoB_{2-x} thin films grown by nonreactive DC magnetron sputtering, J. Vac. Sci. Technol. A 34 (3) (2016) 031511, https://doi.org/10.1116/1.4948234.
[15] C. Fuger, R. Hahn, L. Zauner, T. Wojcik, M. Weiss, A. Limbeck, O. Hunold, P. Polcik, H. Riedl, Anisotropic super-hardness of hexagonal $WB_{2\pm z}$ thin films, Mater. Res. Lett. 10 (2) (2022) 70–77, https://doi.org/10.1080/21663831.2021.2021308.
[16] B. Bakhit, J. Palisaitis, J. Thörnberg, J. Rosen, P.O.Å. Persson, L. Hultman, I. Petrov, J.E. Greene, G. Greczynski, Improving the high-temperature oxidation resistance of TiB_2 thin films by alloying with Al, Acta Mater. 196 (2020) 677–689, https://doi.org/10.1016/j.actamat.2020.07.025.
[17] A.H. Navidi Kashani, S. Mráz, D.M. Holzapfel, M. Hans, L. Löfler, P. Ondračka, D. Primetzhofer, J.M. Schneider, Synthesis and oxidation behavior of $Ti_{0.35}Al_{0.65}B_y$ (y = 1.7–2.4) coatings, Surf. Coat. Technol. 442 (2022) 128190, https://doi.org/10.1016/j.surfcoat.2022.128190.
[18] B. Alling, H. Högberg, R. Armiento, J. Rosen, L. Hultman, A theoretical investigation of mixing thermodynamics, age-hardening potential and electronic structure of ternary $M1_{1-x}M2_xB_2$ alloys with AlB_2 type structure, Sci. Rep. 5 (1) (2015) 9888, https://doi.org/10.1038/srep09888.
[19] J. Thörnberg, S. Mráz, J. Palisaitis, F.F. Klimashin, P. Ondracka, B. Bakhit, P. Polcik, S. Kolozsvari, L. Hultman, I. Petrov, P.O.Å. Persson, J.M. Schneider, J. Rosen, Oxidation resistance and mechanical properties of sputter-deposited $Ti_{0.9}Al_{0.1}B_{2-y}$ thin films, Surf. Coat. Technol. 442 (2022) 128187, https://doi.org/10.1016/j.surfcoat.2022.128187.
[20] A. Mockute, J. Palisaitis, B. Alling, P. Berastegui, E. Broitman, L.Å. Näslund, N. Nedfors, J. Lu, J. Jensen, L. Hultman, J. Patscheider, U. Jansson, P.O.Å. Persson, J. Rosen, Age hardening in $(Ti_{1-x}Al_x)B_{2+\Delta}$ thin films, Scr. Mater. 127 (2017) 122–126, https://doi.org/10.1016/j.scriptamat.2016.09.021.
[21] V. Šroba, T. Fiantok, M. Truchlý, T. Roch, B. Grančič, K. Viskupová, L. Satrapinskyy, P. Švec, Š. Nagy, V. Izai, P. Kúš, M. Mikula, Structure evolution and mechanical properties of Al-alloyed tantalum diboride films prepared by magnetron sputtering co-deposition, J. Vac. Sci. Technol. A 41 (2) (2023) 023410, https://doi.org/10.1116/6.0002390.
[22] C. Hu, S. Lin, M. Podsednik, S. Mráz, T. Wojcik, A. Limbeck, N. Koutná, P. H. Mayrhofer, Influence of co-sputtering AlB_2 to TaB_2 on stoichiometry of non-reactively sputtered boride thin films, Mater. Res. Lett. 12 (8) (2024) 561–570, https://doi.org/10.1080/21663831.2024.2357700.
[23] R. Hahn, V. Moraes, A. Limbeck, P. Polcik, P.H. Mayrhofer, H. Euchner, Electron-configuration stabilized (W,Al)B_2 solid solutions, Acta Mater. 174 (2019) 398–405, https://doi.org/10.1016/j.actamat.2019.05.056.

[24] P. Bliem, S. Mráz, S. Sen, O. Hunold, J.M. Schneider, Self-passivating (Re,Al)B_2 coatings synthesized by magnetron sputtering, Sci. Rep. 8 (1) (2018) 15570, https://doi.org/10.1038/s41598-018-34042-1.

[25] I. Loa, K. Kunc, K. Syassen, P. Bouvier, Crystal structure and lattice dynamics of AlB_2 under pressure and implications for MgB_2, PhysRevB 66 (13) (2002) 134101, https://doi.org/10.1103/PhysRevB.66.134101.

[26] H. Euchner, P.H. Mayrhofer, Designing thin film materials — Ternary borides from first principles, Thin Solid Films 583 (2015) 46–49, https://doi.org/10.1016/j.tsf.2015.03.035.

[27] Y.H. Duan, Y. Sun, Z.Z. Guo, M.J. Peng, P.X. Zhu, J.H. He, Elastic constants of AlB_2-type compounds from first-principles calculations, Comput. Mater. Sci. 51 (1) (2012) 112–116, https://doi.org/10.1016/j.commatsci.2011.07.002.

[28] E. Johansson, F. Eriksson, A. Ektarawong, J. Rosen, B. Alling, Coupling of lattice dynamics and configurational disorder in metal deficient $Al_{1-\delta}B_2$ from first-principles, J. Appl. Phys. 130 (1) (2021) 015110, https://doi.org/10.1063/5.0047275.

[29] K. Liu, X.-L. Zhou, X.-R. Chen, W.-J. Zhu, Structural and elastic properties of AlB_2 compound via first-principles calculations, Phys. B Condens. Matter 388 (1) (2007) 213–218, https://doi.org/10.1016/j.physb.2006.05.428.

[30] A. Jain, S.P. Ong, G. Hautier, W. Chen, W.D. Richards, S. Dacek, S. Cholia, D. Gunter, D. Skinner, G. Ceder, K.A. Persson, Commentary: The Materials Project: A materials genome approach to accelerating materials innovation, APL Mater. 1 (1) (2013) 011002, https://doi.org/10.1063/1.4812323.

[31] U. Burkhardt, V. Gurin, F. Haarmann, H. Borrmann, W. Schnelle, A. Yaresko, Y. Grin, On the electronic and structural properties of aluminum diboride $Al_{0.9}B_2$, J. Solid State Chem. 177 (2) (2004) 389–394, https://doi.org/10.1016/j.jssc.2002.12.001.

[32] M.J. van Setten, M. Fichtner, On the enthalpy of formation of aluminum diboride, AlB_2, J. Alloys. Compd. 477 (1) (2009) L11–L12, https://doi.org/10.1016/j.jallcom.2008.10.025.

[33] A. Grytsiv, P. Rogl, Al-B phase diagrams as published, in: G. Effenberg (Ed.), Diagrams as Published, MSI, Materials Science International Services GmbH, Stuttgart, 2010.

[34] M.L. Whittaker, H.Y. Sohn, R.A. Cutler, Oxidation kinetics of aluminum diboride, J. Solid State Chem. 207 (2013) 163–169, https://doi.org/10.1016/j.jssc.2013.09.028.

[35] K. Nashimoto, Y. Horiguchi, A. Kumatani, T. Okada, Electrochemical catalysis of aluminum diboride thin film fabricated by radio-frequency magnetron sputtering, Jpn. J. Appl. Phys 63 (4) (2024) 04SP24, https://doi.org/10.35848/1347-4065/ad2fde.

[36] T. Glechner, H.G. Oemer, T. Wojcik, M. Weiss, A. Limbeck, J. Ramm, P. Polcik, H. Riedl, Influence of Si on the oxidation behavior of TM-Si-$B_{2\pm z}$ coatings (TM = Ti, Cr, Hf, Ta, W), Surf. Coat. Technol. 434 (2022) 128178, https://doi.org/10.1016/j.surfcoat.2022.128178.

[37] A. Cakara, M. Bonta, H. Riedl, P.H. Mayrhofer, A. Limbeck, Development of a multi-variate calibration approach for quantitative analysis of oxidation resistant Mo–Si–B coatings using laser ablation inductively coupled plasma mass spectrometry, Spectrochim. Acta Part B, At. Spectrosc. 120 (2016) 57–62, https://doi.org/10.1016/j.sab.2016.04.004.

[38] W.C. Oliver, G.M. Pharr, An improved technique for determining hardness and elastic modulus using load and displacement sensing indentation experiments, J. Mater. Res. 7 (6) (1992) 1564–1583, https://doi.org/10.1557/JMR.1992.1564.

[39] A.C. Fischer-Cripps, Critical review of analysis and interpretation of nanoindentation test data, Surf. Coat. Technol. 200 (14) (2006) 4153–4165, https://doi.org/10.1016/j.surfcoat.2005.03.018.

[40] W.D. Westwood, Calculation of deposition rates in diode sputtering systems, J. Vac. Sci. Technol 15 (1) (1978) 1–9, https://doi.org/10.1116/1.569429.

[41] G. Kresse, J. Furthmüller, Efficient iterative schemes for ab initio total-energy calculations using a plane-wave basis set, PhysRevB 54 (16) (1996) 11169–11186, https://doi.org/10.1103/PhysRevB.54.11169.

[42] W. Kohn, L.J. Sham, Self-consistent equations including exchange and correlation effects, PhysRev 140 (4A) (1965) A1133, https://doi.org/10.1103/PhysRev.140.A1133.

[43] J.P. Perdew, K. Burke, M. Ernzerhof, Generalized gradient approximation made simple, PhysRevLett. 77 (18) (1996) 3865–3868, https://doi.org/10.1103/PhysRevLett.77.3865.

[44] D. Gehringer, M. Friák, D. Holec, Models of configurationally-complex alloys made simple, Comput. Phys. Commun. 286 (2023) 108664, https://doi.org/10.1016/j.cpc.2023.108664.

[45] Y. Le Page, P. Saxe, Symmetry-general least-squares extraction of elastic data for strained materials from ab initio calculations of stress, PhysRevB 65 (10) (2002) 104104, https://doi.org/10.1103/PhysRevB.65.104104.

[46] Y. Le Page, P. Saxe, Symmetry-general least-squares extraction of elastic coefficients from ab initio total energy calculations, PhysRevB 63 (17) (2001) 174103, https://doi.org/10.1103/PhysRevB.63.174103.

[47] R. Yu, J. Zhu, H.Q. Ye, Calculations of single-crystal elastic constants made simple, Comput. Phys. Commun. 181 (3) (2010) 671–675, https://doi.org/10.1016/j.cpc.2009.11.017.

[48] J.F. Nye, Physical Properties of Crystals: Their Representation By Tensors And Matrices, Oxford University Press, 1985.

[49] N. Nedfors, O. Vozniy, J. Rosen, Effect of synchronized bias in the deposition of TiB_2 thin films using high power impulse magnetron sputtering, J. Vac. Sci. Technol. A 36 (3) (2018) 031510, https://doi.org/10.1116/1.5003194.

[50] D. Holec, P.H. Mayrhofer, Surface energies of AlN allotropes from first principles, Scr. Mater. 67 (9) (2012) 760–762, https://doi.org/10.1016/j.scriptamat.2012.07.027.

[51] J. Thörnberg, J. Palisaitis, N. Hellgren, F.F. Klimashin, N. Ghafoor, I. Zhirkov, C. Azina, J.-L. Battaglia, A. Kusiak, M.A. Sortica, J.E. Greene, L. Hultman, I. Petrov, P.O.Å. Persson, J. Rosen, Microstructure and materials properties of understoichiometric TiB_x thin films grown by HiPIMS, Surf. Coat. Technol. 404 (2020) 126537, https://doi.org/10.1016/j.surfcoat.2020.126537.

[52] N. Hellgren, A. Sredenschek, A. Petruins, J. Palisaitis, F.F. Klimashin, M.A. Sortica, L. Hultman, P.O.Å. Persson, J. Rosen, Synthesis and characterization of TiB_x ($1.2 \leq x \leq 2.8$) thin films grown by DC magnetron co-sputtering from TiB_2 and Ti targets, Surf. Coat. Technol. 433 (2022) 128110, https://doi.org/10.1016/j.surfcoat.2022.128110.

[53] S.N. Dub, A.A. Goncharov, S.S. Ponomarev, V.B. Filippov, G.N. Tolmacheva, A. V. Agulov, Mechanical properties of $HfB_{2.7}$ nanocrystalline thin films, , J. Superhard Mater. 33 (3) (2011) 151–158, https://doi.org/10.3103/S1063457611030026.

[54] L. Zauner, A. Steiner, T. Glechner, A. Bahr, B. Ott, R. Hahn, T. Wojcik, O. Hunold, J. Ramm, S. Kolozsvári, P. Polcik, P. Felfer, H. Riedl, Role of Si segregation in the structural, mechanical, and compositional evolution of high-temperature oxidation resistant Cr-Si-$B_{2\pm z}$ thin films, J. Alloys. Compd. 944 (2023) 169203, https://doi.org/10.1016/j.jallcom.2023.169203.

[55] A.H. Navidi Kashani, M. Hans, S. Lellig, D.M. Holzapfel, L. Löfler, S. Mráz, D. Primetzhofer, J. Michler, J.M. Schneider, Morphology, mechanical properties, and oxidation behavior of stoichiometric $Ti_{0.33-x}Al_xB_{0.67}$ coatings (x = 0.04, 0.15, 0.21, and 0.28), Acta Mater. 270 (2024) 119829, https://doi.org/10.1016/j.actamat.2024.119829.

[56] T.G. Nieh, J. Wadsworth, Hall-petch relation in nanocrystalline solids, Scripta Metal. Mater. 25 (4) (1991) 955–958, https://doi.org/10.1016/0956-716X(91)90256-Z.

[57] C. Liu, X. Gu, K. Zhang, W. Zheng, Y. Ma, C. Chen, Superhard metallic compound TaB_2 via crystal orientation resolved strain stiffening, PhysRevB 105 (2) (2022) 024105, https://doi.org/10.1103/PhysRevB.105.024105.

[58] M. Stüber, H. Riedl, T. Wojcik, S. Ulrich, H. Leiste, P.H. Mayrhofer, Microstructure of Al-containing magnetron sputtered TiB_2 thin films, Thin Solid Films 688 (2019) 137361, https://doi.org/10.1016/j.tsf.2019.06.011.

[59] P.H. Mayrhofer, C. Mitterer, J.G. Wen, J.E. Greene, I. Petrov, Self-organized nanocolumnar structure in superhard TiB_2 thin films, Appl. Phys. Lett. 86 (13) (2005) 131909, https://doi.org/10.1063/1.1887824.

[60] R.G. Munro, Material properties of titanium diboride, J. Res. Natl. Inst. Stand. Technol. 105 (5) (2000) 709–720, https://doi.org/10.6028/jres.105.057.

[61] X.D. Zhang, G. Sauthoff, Analysis of relationships between cohesive energy, elastic moduli and lattice parameter of some high temperature intermetallics, Intermetallics 3 (2) (1995) 137–140, https://doi.org/10.1016/0966-9795(95)92678-S.

[62] H.S. Kim, M.B. Bush, The effects of grain size and porosity on the elastic modulus of nanocrystalline materials, Nanostruct. Mater. 11 (3) (1999) 361–367, https://doi.org/10.1016/S0965-9773(99)00052-5.

[63] L. Sun, Y. Gao, B. Xiao, Y. Li, G. Wang, Anisotropic elastic and thermal properties of titanium borides by first-principles calculations, J. Alloys. Compd. 579 (2013) 457–467, https://doi.org/10.1016/j.jallcom.2013.06.119.

[64] N. Nedfors, S. Mráz, J. Palisaitis, P.O.Å. Persson, H. Lind, S. Kolozsvari, J. M. Schneider, J. Rosen, Influence of the Al concentration in Ti-Al-B coatings on microstructure and mechanical properties using combinatorial sputtering from a segmented TiB_2/AlB_2 target, Surf. Coat. Technol. 364 (2019) 89–98, https://doi.org/10.1016/j.surfcoat.2019.02.060.

[65] S. Liu, K. Chang, D. Music, X. Chen, S. Mráz, D. Bogdanovski, M. Hans, D. Primetzhofer, J.M. Schneider, Stress-dependent prediction of metastable phase formation for magnetron-sputtered $V_{1-x}Al_xN$ and $Ti_{1-x}Al_xN$ thin films, Acta Mater. 196 (2020) 313–324, https://doi.org/10.1016/j.actamat.2020.06.044.

[66] A.H. Navidi Kashani, S. Lellig, M. Hans, L. Löfler, S. Mráz, P. Schweizer, A. Müller, D. Primetzhofer, J. Michler, J.M. Schneider, Temporally-resolved decomposition of

$Ti_{0.12}Al_{0.21}B_{0.67}$ thin films at 1000 °C, Surf. Coat. Technol. 487 (2024) 131026, https://doi.org/10.1016/j.surfcoat.2024.131026.
[67] R. Jacob, A. Sibley, M. Belusko, M. Liu, J. Quinton, G. Andersson, Investigation into the behaviour of aluminium and steel under melt/freeze cyclic conditions, J. Energy Storage 17 (2018) 249–260, https://doi.org/10.1016/j.est.2018.03.001.
[68] O.A. Golikova, M.M. Kazanin, Z. Mirzazhonov, T. Khomidov, Y.A. Shiyanov, Films of aluminium boride (AlB_{10}), AIP Conf. Proc. 231 (1) (1991) 117–120, https://doi.org/10.1063/1.40882.
[69] Y. Birol, Aluminothermic reduction of boron oxide for the manufacture of Al–B alloys, Mater. Chem. Phys. 136 (2) (2012) 963–966, https://doi.org/10.1016/j.matchemphys.2012.08.030.
[70] H. Okamoto, Al−B (aluminum-boron), J. Phase Equilib. Diffus. 27 (2) (2006) 195–196, https://doi.org/10.1007/s11669-006-0057-4.
[71] G. Will, On the crystal structure of AlB_{10}, J. Am. Chem. Soc 85 (15) (1963) 2335–2336.
[72] J.A. Kohn, G. Katz, A.A. Giardini, AlB_{10}, a new phase, and a critique on the aluminum borides, 111.16. (1959) 53–62, https://doi.org/10.1524/zkri.1959.111.16.53.
[73] H. Duschanek, P. Rogl, The Al-B (aluminum-boron) system, J. Phase Equilibria 15 (5) (1994) 543–552, https://doi.org/10.1007/BF02649415.
[74] T. Nagai, Y. Ogasawara, M. Maeda, Thermodynamic measurement of (Al_2O_3+B_2O_3) system by double Knudsen cell mass spectrometry, J. Chem. Thermodyn. 41 (11) (2009) 1292–1296, https://doi.org/10.1016/j.jct.2009.06.002.
[75] E.M. Levin, C.R. Robbins, H.F. McMurdie, M.K. Reser, Phase diagrams for ceramists, Am. Ceram. Soc. (1964) 136.
[76] A. Bahr, O. Beck, T. Glechner, A. Grimmer, T. Wojcik, P. Kutrowatz, J. Ramm, O. Hunold, S. Kolozsvári, P. Polcik, E. Ntemou, D. Primetzhofer, H. Riedl, Quaternary diborides—improving the oxidation resistance of $TiB_{2\pm z}$ coatings by disilicide alloying, Mater. Res. Lett. 11 (9) (2023) 733–741, https://doi.org/10.1080/21663831.2023.2225554.